Appendix A. Supplementary methods

Appendix A.1. Constrained MNE

The GCS considered in this paper was based on an explicit model of spatial leakage geometry applicable to any linear source reconstruction. In this appendix, we describe an alternative derivation in the special case of MNE.

Mathematically, the inverse operator $\boldsymbol{W}$ of MNE corresponds to the minimum of the function

$$\mathcal{F}(\boldsymbol{W}) = \tfrac{1}{2}\,\mathsf{tr}\left[(\boldsymbol{W}\boldsymbol{L}-\boldsymbol{1}_N)(\boldsymbol{W}\boldsymbol{L}-\boldsymbol{1}_N)^{\mathsf{T}} + \kappa\,\boldsymbol{W}\boldsymbol{C}_\varepsilon\boldsymbol{W}^{\mathsf{T}}\right], \tag{A.1}$$

where $\boldsymbol{1}_N$ denotes the $N\times N$ identity matrix (Backus and Gilbert, 1970; Tarantola, 2004). Keeping in mind property *(v)* from the Theory section, let us rather look for the minimum $\boldsymbol{W}'$ of this function under the constraint that the PSF of the seed s_0 vanishes, $\boldsymbol{W}'L_{s_0}=0$. This amounts to extremize the expression $\mathcal{F}(\boldsymbol{W}')+\lambda^{\mathsf{T}}\boldsymbol{W}'L_{s_0}$, where λ represents a $(N\times 1)$ Lagrange multiplier. After some algebra, the variational equation for $\boldsymbol{W}'$ reads

$$\boldsymbol{W}' = (\boldsymbol{L}^{\mathsf{T}} - \lambda L_{s_0}^{\mathsf{T}})\,(\boldsymbol{L}\boldsymbol{L}^{\mathsf{T}} + \kappa\,\boldsymbol{C}_\varepsilon)^{-1}\,. \tag{A.2}$$

Recognizing the basic MNE inverse operator $\boldsymbol{W}$ (recovered by formally setting $\lambda=0$), we obtain

$$\boldsymbol{W}' = \boldsymbol{W} - \lambda W_{s_0}\,. \tag{A.3}$$

Finally, imposing the constraint $\boldsymbol{W}'L_{s_0}=0$ allows to solve for the multiplier, $\lambda = \boldsymbol{W}L_{s_0}/W_{s_0}L_{s_0}$, hence demonstrating that $\boldsymbol{W}'=\boldsymbol{W}^{\mathrm{GCS}}$ (see the Theory section in the main text).

The above constrained minimization is actually part of a class of problems considered in the DeFleCT algorithm (Hauk and Stenroos, 2014). The GCS for MNE can thus also be viewed as a special case of DeFleCT, although that is not true for general linear inverse operators.

Appendix A.2. Unbiased prior for MNE regularization

In this appendix, we derive the formula used in this paper for the regularization parameter κ, i.e.,

$$\kappa = \frac{\mathsf{tr}\left(\boldsymbol{C}_\varepsilon^{-1}\boldsymbol{L}\boldsymbol{L}^{\mathsf{T}}\right)}{\mathsf{tr}\left(\boldsymbol{C}_\varepsilon^{-1}\boldsymbol{C}_\mu\right) - M}\,, \tag{A.4}$$

via a consistency argument with the prior model assumptions underlying MNE.

Physically, MNE relies on the hypothesis that sources ψ and noise ε are uncorrelated gaussian white noises with respective covariances $\kappa^{-1}\boldsymbol{1}_N$ and $\boldsymbol{C}_\varepsilon$ (Baillet et al., 2001; Tarantola, 2004). The observed data μ are supposed to be related to these stochastic processes via the forward model $\mu = \boldsymbol{L}\,\psi+\varepsilon$. (The expression $2\mathcal{F}/\kappa$ minimized in Appendix A.1 thus corresponds to the variance of the reconstruction error $\boldsymbol{W}\mu-\psi = (\boldsymbol{W}\boldsymbol{L}-\boldsymbol{1}_N)\psi+\boldsymbol{W}\varepsilon$.) Direct computation of the *a priori* data covariance $\boldsymbol{C}_\mu$ then yields

$$\boldsymbol{C}_\mu = \kappa^{-1}\boldsymbol{L}\boldsymbol{L}^{\mathsf{T}} + \boldsymbol{C}_\varepsilon\,. \tag{A.5}$$

This equation is at the basis of the sLORETA normalization (see the Theory section), which estimates sources noise variance from its projections $\hat{\lambda}_s^2 = W_s\boldsymbol{C}_\mu W_s^{\mathsf{T}}$ (Pascual-Marqui, 2002; Sekihara et al., 2005). We use it here to derive a self-consistent formula for κ in terms of the SNR estimate $\zeta = \frac{1}{M}\,\mathsf{tr}\,(\boldsymbol{C}_\varepsilon^{-1}\boldsymbol{C}_\mu)$ defined in the main text. Indeed, the above equation (A.5) directly implies $\zeta = \frac{1}{M\kappa}\mathsf{tr}\,(\boldsymbol{C}_\varepsilon^{-1}\boldsymbol{L}\boldsymbol{L}^{\mathsf{T}}) + 1$. Therefore, assuming ζ known, the regularization parameter can be expressed as

$$\kappa = \frac{\mathsf{tr}\left(\boldsymbol{C}_\varepsilon^{-1}\boldsymbol{L}\boldsymbol{L}^{\mathsf{T}}\right)}{M\big(\zeta-1\big)}\,. \tag{A.6}$$

Plugging the explicit definition of ζ into this result yields the promised equation (A.4). This formula has the advantage of being both unbiased with respect to the MNE priors and invariant under coordinate changes in sensor space.

Another analytical expression for κ as function of the SNR is given in Hämäläinen et al. (2010) using specific sensor coordinates, i.e., whitened data. When correctly written in invariant terms, this expression actually reads $\kappa = \frac{1}{M\zeta}\mathsf{tr}\,(\boldsymbol{C}_\varepsilon^{-1}\boldsymbol{L}\boldsymbol{L}^{\mathsf{T}})$ and thus bears close resemblance with (A.6). This formula is biased in the sense that it neglects the contribution of noise covariance in (A.5) and is thus inconsistent with the MNE priors, especially in the low SNR limit $\zeta\to 1$. In practice, however, the resting-state and auditory-motor data always led to $\zeta\geq 2$.

Appendix A.3. Algorithm for network simulations

In this appendix, we describe the two-step method used to generate pairs of signals with given values of linear and non-linear (slow envelope) correlations. Our starting point is the Hilbert decomposition of time series x and y with narrow-band spectrum (i.e., $\Delta\nu \ll \nu_0$ for band center ν_0 and half-width $\Delta\nu$),

$$x_t = a_t\,\cos(2\pi\nu_0 t + \alpha_t)\,, \tag{A.7}$$

$$y_t = b_t\,\cos(2\pi\nu_0 t + \beta_t)\,, \tag{A.8}$$

with $0<t\leq T$. For such signals, the Hilbert envelopes (a, b) and phases (α, β) fluctuate slowly, with temporal variation rates bounded by $\Delta\nu$. In our simulations, these signals were generated from β-band ($\nu_0 = 16.5\,\mathrm{Hz}$, $\Delta\nu = 4.5\,\mathrm{Hz}$) filtered white noises whereas a was replaced by a positive oscillation $a_t = 1.5+\sin(2\pi\nu_a t)$ with very slow frequency $\nu_a<\Delta\nu$ ($\nu_a = 0.1\,\mathrm{Hz}$).

Since a and b are uncorrelated time series, envelope correlation $\mathsf{corr}(a,b)$ can first be set to value r_{env} in a standard way by substituting b with the linear combination $b+ka$, where

$$k = \frac{r_{\mathrm{env}}}{\sqrt{1-r_{\mathrm{env}}^2}}\,\frac{\sigma_b}{\sigma_a}\,. \tag{A.9}$$

To fix the *slow* envelope correlation, the temporal standard deviations σ_a and σ_b must be computed after low-pass filtering a and b below some frequency ν_{env} with $\nu_a < \nu_{\text{env}} < \Delta\nu$. We used $\nu_{\text{env}} = 1\,\text{Hz}$.

The linear correlation of the resulting signals (whose envelopes a, b are now correlated but independent of phases α, β) can then be set by modulating their phase coupling. The method relies on the following "Hilbert decomposition" formula for linear correlation (derived below):

$$\mathsf{corr}(x,y) = \frac{\langle a_t b_t\rangle}{\sqrt{\langle a_t^2\rangle\langle b_t^2\rangle}}\left\langle \cos(\beta_t - \alpha_t)\right\rangle, \tag{A.10}$$

the brackets denoting temporal averaging. Linear correlation can thus be fixed to value r_{lin} by controlling the signals phase coupling measure $\langle\cos(\beta_t - \alpha_t)\rangle$. In our simulations, we replaced β by $\alpha + \theta$ with constant phase lag $0 \leq \theta < \pi$ satisfying

$$\cos\theta = \frac{r_{\text{lin}}\sqrt{\langle a_t^2\rangle\langle b_t^2\rangle}}{\langle a_t\, b_t\rangle}\,. \tag{A.11}$$

In the absence of linear correlation, we have $\theta = \pi/2$, so the simulated signals conform to the temporal assumptions of both static and instantaneous orthogonalizations.

For completeness, let us derive the decomposition formula (A.10). First, using the zero-mean property of narrow-band signals and the independence of envelopes and phases, the covariance of x and y reads

$$\begin{aligned}\langle x_t y_t\rangle &= \langle a_t b_t\rangle\left\langle \cos(2\pi\nu_0 t + \alpha_t)\cos(2\pi\nu_0 t + \beta_t)\right\rangle \\ &= \tfrac{1}{2}\langle a_t b_t\rangle\left\langle \cos(\beta_t - \alpha_t) + \cos(4\pi\nu_0 t + \alpha_t + \beta_t)\right\rangle.\end{aligned} \tag{A.12}$$

For long time ($\nu_0 T \gg 1$), the term $\langle\cos(4\pi\nu_0 t + \alpha_t + \beta_t)\rangle$ converges to $\langle\cos(4\pi\nu_0 t)\rangle = 0$ because the temporal averaging is dominated by the high-frequency ($2\nu_0$) oscillation, so

$$\langle x_t y_t\rangle = \tfrac{1}{2}\langle a_t b_t\rangle\left\langle \cos(\beta_t - \alpha_t)\right\rangle. \tag{A.13}$$

Furthermore, we obtain the signals variance $\langle x_t^2\rangle = \langle a_t^2\rangle/2$ and $\langle y_t^2\rangle = \langle b_t^2\rangle/2$ by setting $x = y$. Finally, plugging these results into the definition $\mathsf{corr}(x,y) = \langle x_t y_t\rangle/(\langle x_t^2\rangle\langle y_t^2\rangle)^{1/2}$ leads to the sought formula (A.10).

Appendix B. Supplementary results

Appendix B.1. Structural effects on noisy point-spread functions (auditory seed)

Figure S1 depicts the results of the PSF dissimilarity analyses for the geometric correction from the left A1 seed. Results were similar to the correction from SM1ha, despite the fact that the MEG signal originating from the SM1 cortex has higher SNR than from the A1 cortex (the latter being located deeper within the sylvian sulcus). In particular, the respective plots of PSF dissimilarity versus distance to the seed (Figures 2A and S1A, middle) as well as the effect of data SNR and lead field errors (Figures 2C and S1C) are comparable. In the examples shown in Figure S1B, it is noteworthy that the effect of the GCS on the PSF at the SMG (2 cm away from the A1 seed) was mild enough, in the sense that the local PSF maximum correction was still located in the SMG.

Furthermore, both examples illustrated some longer-range spatial leakage effect (from the A1 cortex to the lower bank of the temporal lobe and the cerebellum) that was eliminated after geometric correction. This was also seen at the level of FC estimation in Figures 4 and 5B (bottom left).

Appendix B.2. Example of seed mislocation effect associated with the auditory seed

Figure S2 shows the effect of seed mislocation on reconstructed FC maps for a simulated binodal network of orthogonal signals involving the left and right A1 cortices, with the used seed misplaced by 1.5 cm in the STG. Results parallel those of the analogous simulation shown in Figures 3D and S3D. Briefly, seed mislocation generated a local FC pattern that dominated after the GCS and persisted after the signal orthogonalization (but with a significant decrease compared to the GCS).

Appendix B.3. Spatial leakage correction for simulated binodal networks (uncoupled signals)

Figure S3 illustrates the results of geometric correction for simulated pairs of active but uncoupled nodes. Strongly significant spatial leakage FC (T_9-maps maximum > 130) was observed in all considered cases. Without seed mislocation (Figure S3A–C), the GCS completely eliminated FC, even for very close nodes (0.5 cm, Figure S3C). With seed mislocation, a spurious FC pattern remained significant after correction (Figure S3D).

Appendix B.4. Signal orthogonalization for simulated binodal networks (orthogonal signals)

Figure S4 shows the results of signal orthogonalization for the network simulations considered in Figure 3. Patterns of spatial leakage FC were qualitatively similar to those obtained with the GCS, including the presence of spurious local FC in the case of nearby nodes (distance < 2 cm, Figure S3B, C, left) and seed mislocation (Figure S4D, left). This convergence of results can be explained by the nature of the simulation, where the nodes signals satisfy the assumptions of static and instantaneous orthogonalizations, i.e., no linear correlation (Brookes et al., 2012) and phase lag fixed at $\pi/2$ (Hipp et al., 2012), respectively (see Appendix A.3 for details).

Direct comparison of correction methods (Figure S4, right) revealed no significant differences in the ideal case of remote nodes without seed mislocation (Figure S4A, right). In the other cases, static orthogonalization significantly decreased local FC estimation compared to the

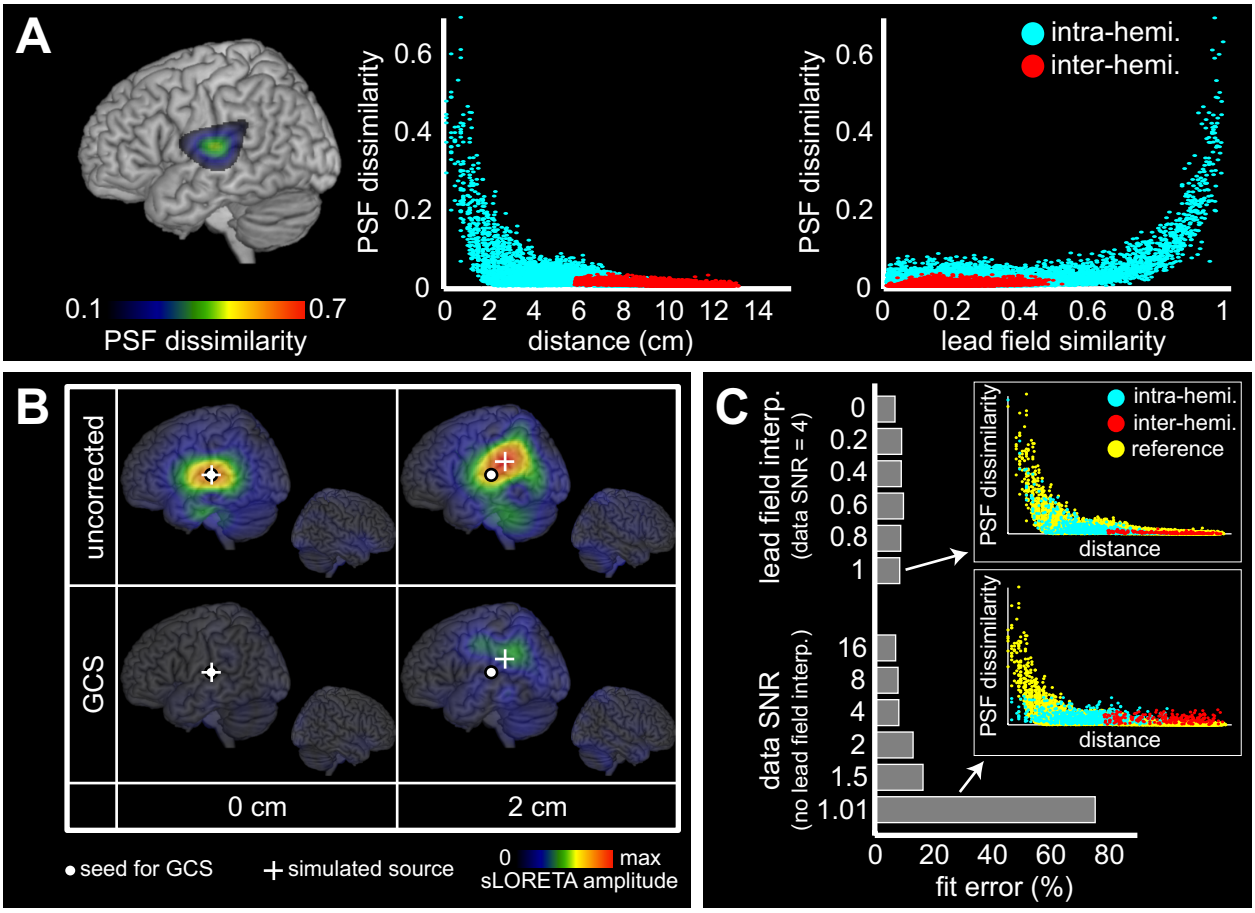

Figure S1: *Effect of the GCS from the left A1 cortex on noisy PSFs.* **A:** Spatial distribution of PSF dissimilarity for the reference simulation (SNR $\zeta = 4$, no lead field error), represented as a cortical map (*left*) and plotted against distance (*middle*) or lead field similarity (*right*) between the seed and the simulated node. Blue and red points respectively denote sources in the left and the right hemispheres. **B:** Example PSFs before (*top*) and after (*bottom*) geometric correction taken from the reference simulation with simulated node (white cross) placed either at the seed (white dot) or at the SMG (2 cm away). Maps were normalized using sLORETA for visualization. **C:** Effect of parameters variation on PSF dissimilarity, as assessed by the fit error to the reference simulation. Inserts show two examples with explicit comparison to the reference simulation (yellow points).

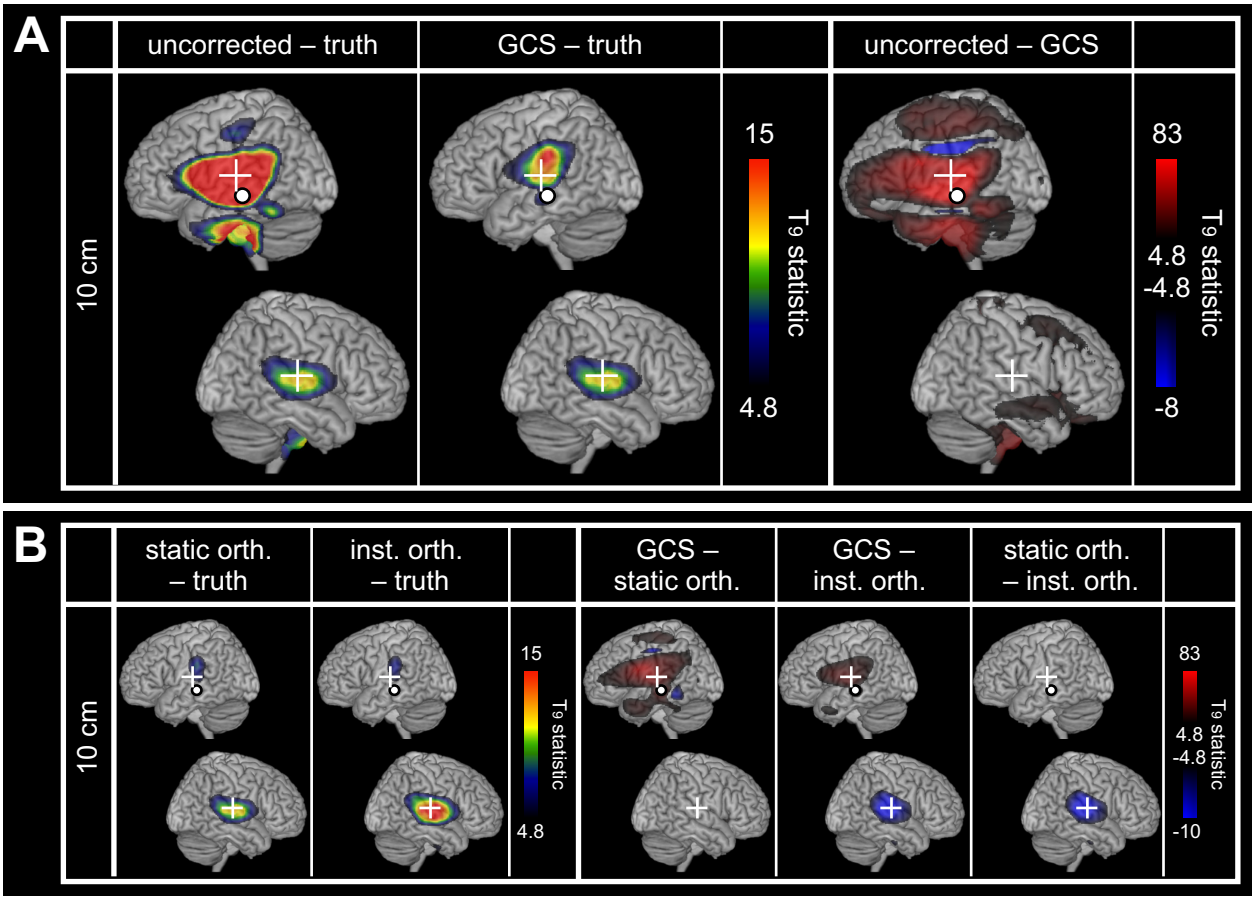

Figure S2: *Spatial leakage correction for a simulated binodal network (orthogonal signals) with left A1 seed mislocation.* The statistical maps assess spatial leakage FC for uncorrected and corrected slow envelope FC estimations as well as the differential effect of corrections. Network nodes are indicated by white crosses, whereas the white dot shows the seed location used for FC mapping and spatial leakage correction. Statistical thresholding was applied at FWE-corrected significance level 0.05. Positive upper scales were set to the maximum of the GCS − truth (**A**, *middle*) or uncorrected − GCS (**A**, *right*) map, while negative lower scales were set arbitrarily for visualization.

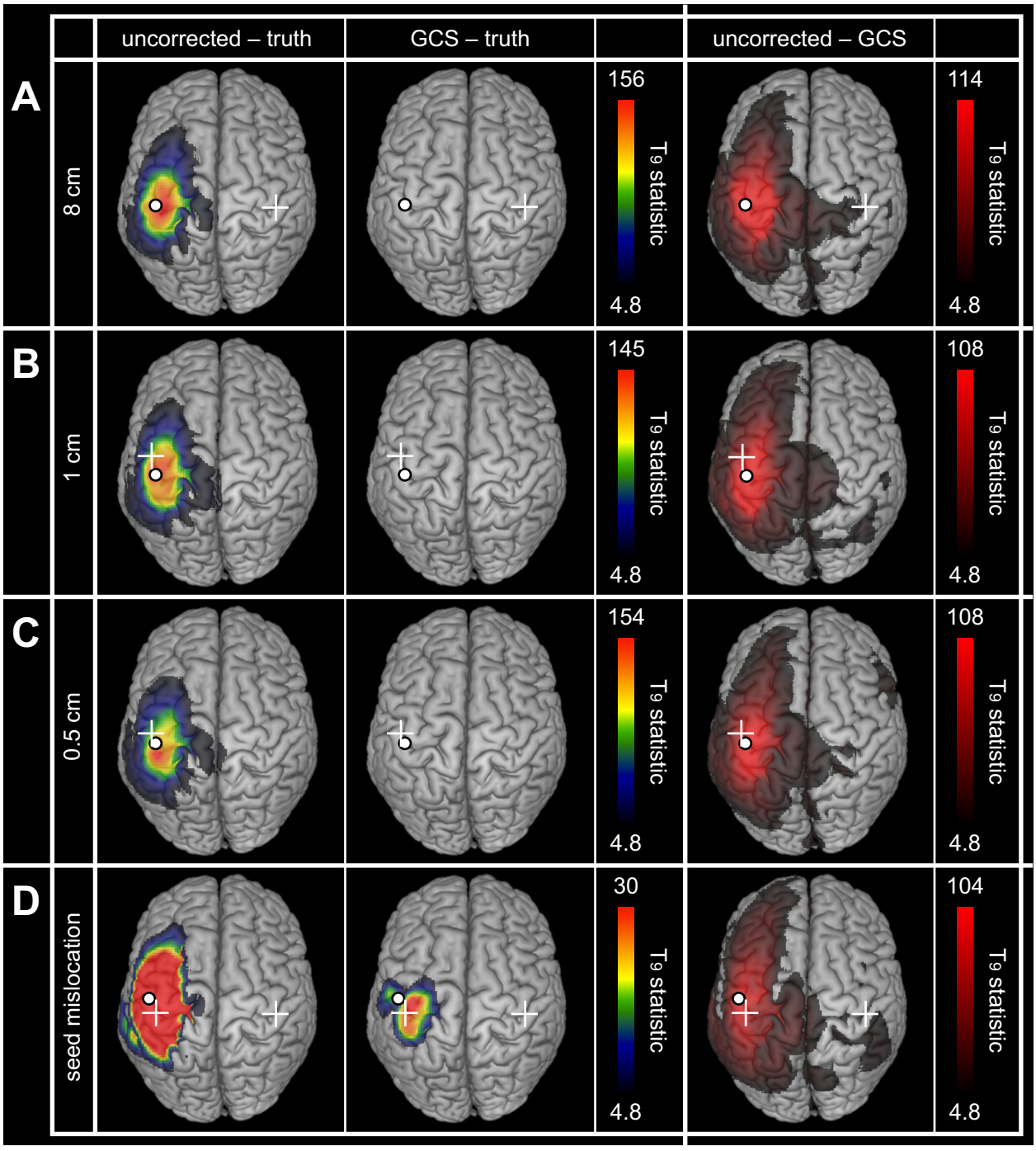

Figure S3: *Geometric correction for simulated binodal networks (uncoupled signals).* The statistical maps assess spatial leakage FC for uncorrected (*left*) and corrected (*middle*) slow envelope FC estimations as well as the differential effect of the GCS (*right*). Network nodes are indicated by the white dot and cross (**A**–**C**) or two white crosses (**D**). In all cases, the white dot shows the seed location used for FC mapping and geometric correction. Statistical thresholding was applied at FWE-corrected significance level 0.05, while upper scales were set to the maximum of the uncorrected − truth (**A**–**C**, left and middle), GCS − truth (**D**, left and middle) or uncorrected − GCS (right) maps.

GCS (Figure S4B–D, right). Accordingly, instantaneous orthogonalization significantly decreased the spurious local FC involved in seed mislocation (Figure S4D, right) but significantly increased FC estimation at target node locations (Figure S4B, D, right). A mechanism for this overestimation effect is given in Wens (2015). Finally, comparing both orthogonalization methods showed significantly lower FC for static than for instantaneous orthogonalizations (Figure S4B, D, right).

Appendix B.5. Differential effects of spatial leakage corrections for simulated multinodal networks

Figure S5 reports the statistical comparison of spatial leakage corrections for the multinodal network simulations considered in Figure 4. The GCS significantly decreased FC estimation over large regions of the brain (Figure S5, left) and significantly increased FC estimation of the inter-hemispheric A1 coupling (Figure S5, bottom left). Signal orthogonalization underestimated FC compared to the GCS, except for the inter-hemispheric SM1 coupling that was overestimated by instantaneous orthogonalization. (The latter effect was also observed for the binodal network simulations, see Appendix B.4.) Finally, comparison of both orthogonalization methods showed no significant differences except for the inter-hemispheric A1 coupling, which was indeed absent using static orthogonalization (Figure 4).

Appendix B.6. Differential effects of spatial leakage corrections for auditory-motor network

Figure S6 shows the significant differences induced by spatial leakage corrections. The resulting maps did not disclose extensive regions, presumably because of substantial inter-subjects variability in this coherence analysis.

References for Supplementary Materials

Backus, G., Gilbert, F., 1970. Uniqueness in the inversion of inaccurate gross Earth data. Phil. Trans. R. Soc. Lond. A 266, 123–192. doi:10.1098/rsta.1970.0005.

Baillet, S., Mosher, J.C., Leahy, R.M., 2001. Electromagnetic brain mapping. IEEE Sig. Proc. Mag. 18, 14–30. doi:10.1109/79.962275.

Brookes, M.J., Woolrich, M., Barnes, G.R., 2012. Measuring functional connectivity in MEG: a multivariate approach insensitive to linear source leakage. NeuroImage 63, 910–920. doi:10.1016/j.neuroimage.2012.03.048.

Hämäläinen, M., Lin, F., Mosher, J., 2010. Anatomically and functionally constrained minimum-norm estimates, in: Hansen, P.C., Kringelbach, M.L., Salmelin, R. (Eds.), MEG–an introduction to methods. Oxford University Press, pp. 186–215.

Hauk, O., Stenroos, M., 2014. A framework for the design of flexible cross-talk functions for spatial filtering of EEG/MEG data: DeFleCT. Human Brain Mapping 35, 1642–1653. doi:10.1002/hbm.22279.

Hipp, J.F., Hawellek, D.J., Corbetta, M., Siegel, M., Engel, A.K., 2012. Large-scale cortical correlation structure of spontaneous oscillatory activity. Nat. Neurosci. 15, 884–890. doi:10.1038/nn.3101.

Pascual-Marqui, R.D., 2002. Standardized low-resolution brain electromagnetic tomography (sLORETA): technical details. Methods Find. Exp. Clin. Pharmacol. 24 Suppl D, 5–12.

Sekihara, K., Sahani, M., Nagarajan, S.S., 2005. Localization bias and spatial resolution of adaptive and non-adaptive spatial filters for MEG source reconstruction. NeuroImage 25, 1056–1067. doi:http://dx.doi.org/10.1016/j.neuroimage.2004.11.051.

Tarantola, A., 2004. Inverse Problem Theory and Methods for Model Parameter Estimation. SIAM.

Wens, V., 2015. Investigating complex networks with inverse models: Analytical aspects of spatial leakage and connectivity estimation. Phys. Rev. E 91, 012823. doi:10.1103/PhysRevE.91.012823.

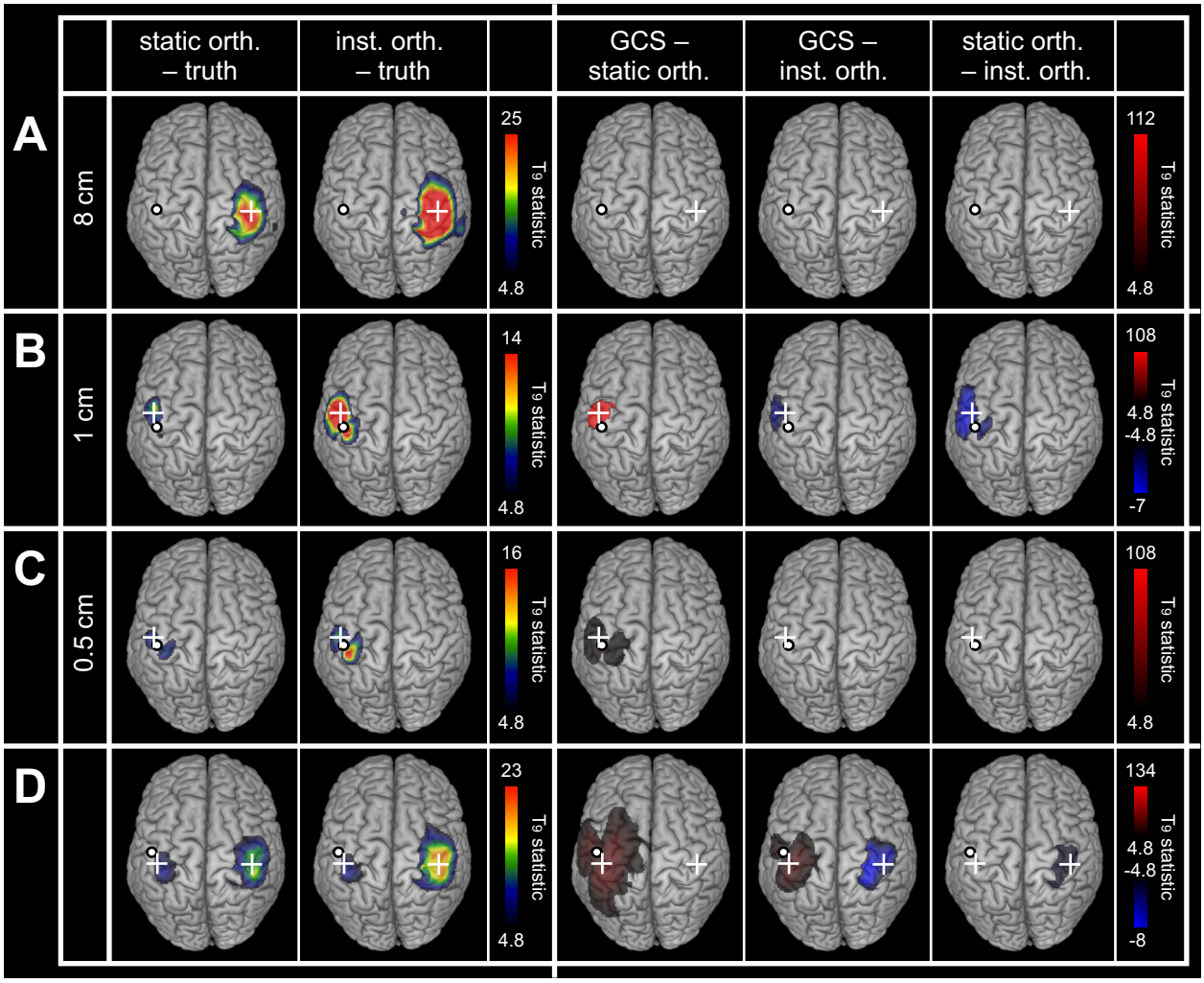

Figure S4: *Signal orthogonalization and comparison of spatial leakage corrections for simulated binodal networks (orthogonal signals).* The statistical maps assess spatial leakage FC for orthogonalized slow envelope FC estimations (*left*) as well as the differential effect of the GCS, static and instantaneous orthogonalizations (*right*). Network nodes are indicated by the white dot and cross (**A**–**C**) or two white crosses (**D**). In all cases, the white dot shows the seed location used for FC mapping and spatial leakage correction. Statistical thresholding was applied at FWE-corrected significance level 0.05. Positive upper scales were set to the maximum of the GCS − truth (left) or uncorrected − GCS (right) maps (see Figure 3), while negative lower scales were set arbitrarily for visualization.

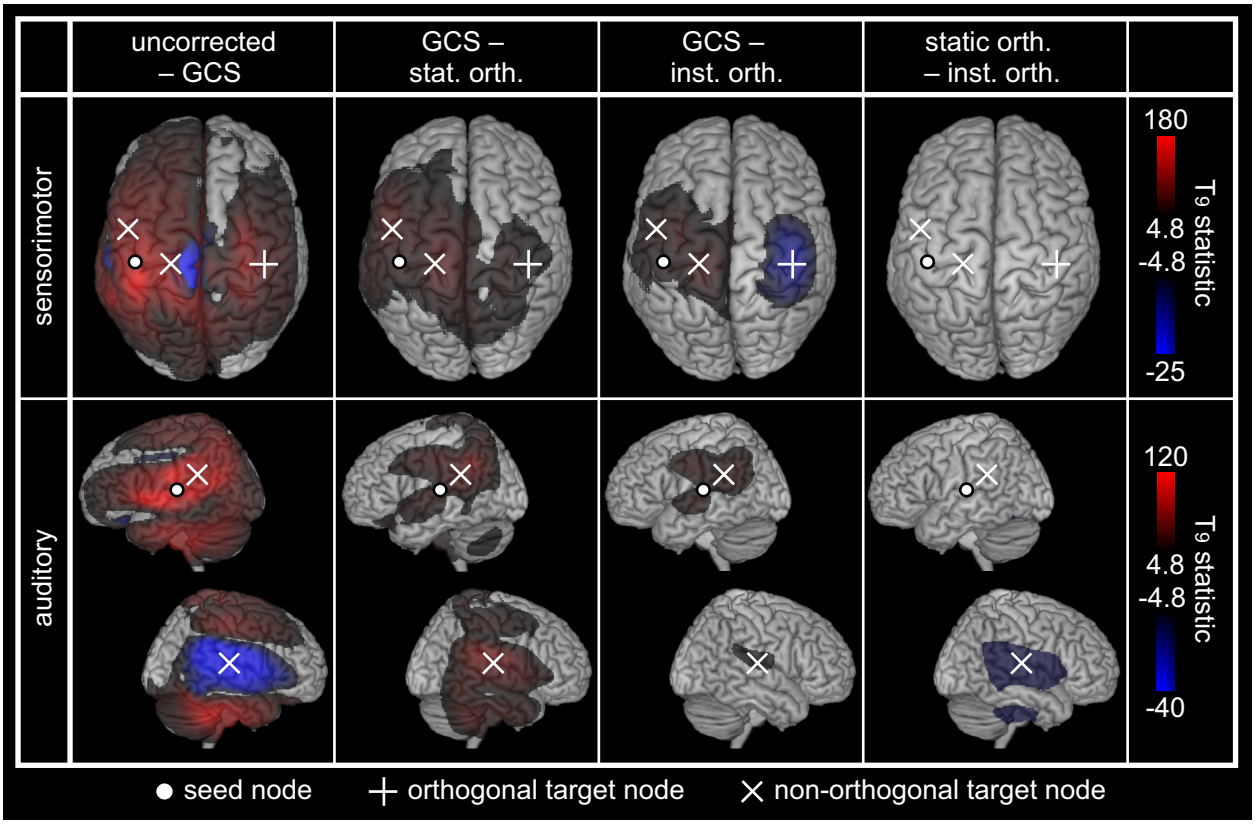

Figure S5: *Differential effects of spatial leakage corrections for simulated multinodal networks.* The statistical maps compare spatial leakage corrections (uncorrected, GCS, static and instantaneous orthogonalizations) on slow envelope FC. Network nodes are indicated by white dots (seed node, also used for FC mapping and spatial leakage correction) and crosses (target node; +: orthogonal, ×: non-orthogonal). Statistical thresholding was applied at FWE-corrected significance level 0.05. Positive upper scales were set to the maximum of the uncorrected − GCS maps, while negative lower scales were set arbitrarily for visualization.

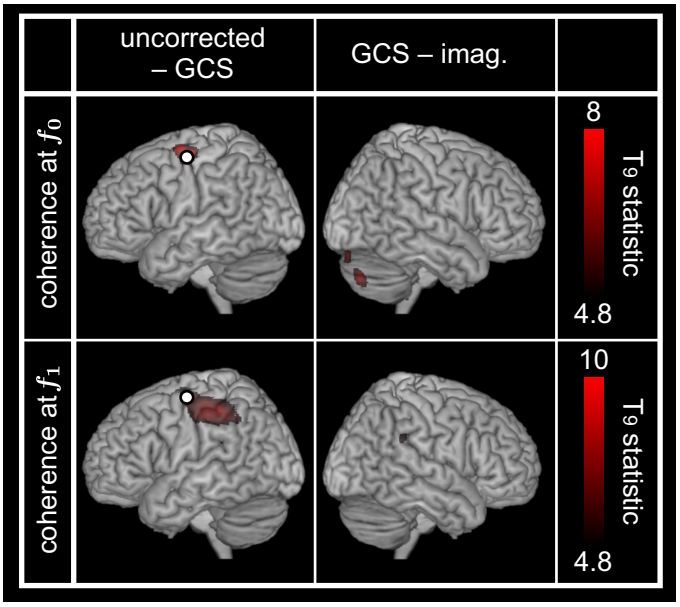

Figure S6: *Differential effects of spatial leakage corrections for auditory-motor network.* The statistical maps compare spatial leakage corrections (uncorrected, GCS and imaginary coherence) on task-based cortico-cortical coherence at f_0 (*top*) and f_1 (*bottom*). Statistical thresholding was applied at FWE-corrected significance level 0.05, and upper scales were set to the maximum of the uncorrected − GCS maps. In all cases, the white dot indicates the seed used for FC mapping and spatial leakage correction. The hemispheres not shown did not disclose significant regions.